Northumbria Research Link

Citation: Luo, Minghe, Wang, Caiyun, Lu, Haotian, Lu, Yunhao, Xu, Ben Bin, Sun, Wenping, Pan, Hongge, Yan, Mi and Jiang, Yinzhu (2021) Dendrite-free zinc anode enabled by zinc-chelating chemistry. Energy Storage Materials, 41. pp. 515-521. ISSN 2405-8297

Published by: Elsevier

URL: https://doi.org/10.1016/j.ensm.2021.06.026 <https://doi.org/10.1016/j.ensm.2021.06.026>

This version was downloaded from Northumbria Research Link: https://nrl.northumbria.ac.uk/id/eprint/46490/

Northumbria University has developed Northumbria Research Link (NRL) to enable users to access the University's research output. Copyright © and moral rights for items on NRL are retained by the individual author(s) and/or other copyright owners. Single copies of full items can be reproduced, displayed or performed, and given to third parties in any format or medium for personal research or study, educational, or not-for-profit purposes without prior permission or charge, provided the authors, title and full bibliographic details are given, as well as a hyperlink and/or URL to the original metadata page. The content must not be changed in any way. Full items must not be sold commercially in any format or medium without formal permission of the copyright holder. The full policy is available online: http://nrl.northumbria.ac.uk/policies.html

This document may differ from the final, published version of the research and has been made available online in accordance with publisher policies. To read and/or cite from the published version of the research, please visit the publisher's website (a subscription may be required.)

Northumbria University NEWCASTLE

University Library

Dendrite-free zinc anode enabled by zinc-chelating chemistry

Minghe Luo[1], Caiyun Wang[1], Haotian Lu[1], Yunhao Lu[2], Ben Bin Xu[3], Wenping Sun[1], Hongge Pan[1,4], Mi Yan[1], Yinzhu Jiang[1,5]*

[1]School of Materials Science and Engineering, State Key Laboratory of Clean Energy Utilization, Zhejiang University, Hangzhou 310027, P.R. China

[2]Department of Physics, Zhejiang Province Key Laboratory of Quantum Technology and Device, Zhejiang University, Hangzhou 310027, P.R. China

[3]Smart Materials and Surfaces Lab, Mechanical Engineering, Faculty of Engineering and Environment, Northumbria University, Newcastle upon Tyne NE1 8ST, UK

[4]Institute of Science and Technology for New Energy, Xi'an Technological University, Xi'an 710021, P.R. China

[5]ZJU-Hangzhou Global Scientific and Technological Innovation Centre, Zhejiang University, Hangzhou, 311200, P.R. China

E-mail: yzjiang@zju.edu.cn

Acknowledgements

This work is supported by National Natural Science Foundation of China (51722105), National Key Research and Development Program (2019YFE0111200) and Zhejiang Provincial Natural Science Foundation of China (LR18B030001).

Competing interests

The authors declare no competing financial interests.

Dendrite-free zinc anode enabled by zinc-chelating chemistry

Keywords: zinc ion battery, metal anode, chelating chemistry, deposition kinetic, dendrite growth

ABSTRACT: Rechargeable aqueous Zn-ion battery has been considered as a key complement to the existing battery technologies due to its intrinsic merits such as operational safety and cost saving. However, issues of dendrite growth and accompanied water consumption hinder its further development. In this work, we utilize a chelating agent, 2-Bis(2-hydroxyethyl) amino-2-(hydroxymethyl)-1,3-propanediol (BIS-TRIS), to regulate the solvation sheath structure of Zn^{2+}. Benefiting from such zinc-chelating coordination, Zn^{2+} 2D diffusion can be restricted and the altered deposition kinetic has contributed to the inhibition of the dendrite growth. In addition, partial substitution of water in solvation shell with chelator can also greatly suppress the competitive hydrogen evolution reaction (HER). Consequently, a stable symmetric Zn cell with lifetime more than 1000 h at a current density of 1 mA cm^{-2} is achieved. Moreover, the aqueous Zn/MnO_2 battery with BIS-TRIS as electrolyte additive delivers an 86% capacity retention after 600 cycles at 500 mA g^{-1}. This zinc-chelating coordination based facile strategy opens a new window for the future development in dendrite-free Zn anode.

1. Introduction

Zn-based battery has attracted significant attentions recently, due to its appealing intrinsic merits, *e.g.* low toxicity, intrinsic safety, cost-effectiveness and high theoretical capacity (820 mAh g^{-1} or 5855 mAh cm^{-3}). [1] [2] [3] [4] Zn-Mn batteries still dominate the primary battery market to date. [5] However, with the growing of renewable energy power generation technology, the application of energy storage and conversion devices, especially rechargeable battery system,

has already become the target. [6] [7] [8] [9]The proposal of rechargeable Zn-based battery concept can be traced back to 1980, but more attention was concentrated on alkaline zinc cell at that time.[10] [11] [12] In 2012, the rechargeable Zn-based battery concept was reformed, accompanied by the interesting discovery on the Zn^{2+} intercalation in $ZnSO_4$ system with α-MnO_2 as cathode, thus leading to a unique battery system named Zinc ion battery (ZIB). [13] [14] [15]

Currently, rechargeable Zn-ion battery using neutral or mildly acidic electrolyte is in a new round of boom. While the corrosive alkaline condition is avoided, a grand challenge remains in terms of achieving a good electrochemistry reversibility on Zn anode, where heavy setbacks can be caused by severe dendrite growth and poor electrochemical stability. [16] [17] [18] The undesirable dendrite can not only penetrate the separator causing inner short circuit, but also detach from electrode to yield inefficiency and irreversibility of battery. [19] [20] Meanwhile, the absence of compact solid electrolyte interphase (SEI), a functional layer to protect the metal anode from electrolyte, also make the emergence of competitive hydrogen evolution unavoidably during the zinc deposition. [21] [22] The subsequent local accumulation of OH^- further passivates the Zn anode by forming Zn^{2+}-insulating by-products on the surface, which also aggravates the formation of dendrite. [23] Thus, to enable the transition from laboratory to scale up application, the inhibition of dendrite growth and side reactions is needed to be fulfilled when designing long-life and high-performance ZIBs.

Among the recent technical explorations to facilitate reversible Zn anode, modulating zinc coordination environment through electrolyte optimization has been demonstrated as an effective strategy. Wang *et al.* proposed a new concept of "water-in-salt" aqueous electrolyte for ZIB, which contains high concentration salt in water (typically molality>20 m). [24] In such highly concentrated electrolyte, the solvation sheath of Zn^{2+} is primarily occupied by salt anions rather than typically six water coordinated Zn^{2+} structure in the dilute electrolyte ($(Zn(OH_2)_6)^{2+}$). The altered coordination environment avoids the direct contact of metal anode with H_2O in solvation sheath structure, which greatly suppress the hydrogen evolution reaction (HER) and

the formation of by-products. However, the highly soluble fluorinated-based salt is costly, especially in the case of high concentration up to 20 M. Recently, Pan *et al.* demonstrated a highly reversible Zn anode by employing 68 vol% ethylene glycol (EG) hybrid electrolyte. [25] In such electrolyte, the coordination environment of Zn^{2+} is transformed from $[Zn(OH_2)_6]^{2+}$ into $[Zn(OH_2)_m(EG)_n]^{2+}$. However, the flammability of alcohols has been a concern of safety and such mixed electrolyte also posed challenge for solvent recycle. The search for effective technical route to realize reversible Zn anode is an ongoing mission.

From the point of view in regulating solvation structure of Zn^{2+}, a new strategy is proposed based on chelating chemistry through leveraging the interaction between the metal ion and chelator. A highly reversible Zn anode is achieved based on 2-Bis(2-hydroxyethyl) amino-2-(hydroxymethyl)-1,3-propanediol (denoted as BIS-TRIS) as electrolyte chelating additive. As shown in **Figure 1**a, the molecule is rich in hydroxyl groups containing oxygen lone-pair electrons and has one tertiary amine group, all of which are expected to complex with Zn^{2+} to regulate the solvation structure. [26] According to the literature by Helmut *et al*. which reports the metal-ion-coordinating properties of BIS-TRIS, the participation of the hydroxyl groups of BIS-TRIS is high in complex $Zn(BIS\text{-}TRIS)^{2+}$ formation with at least two hydroxyl groups involved. It is undoubtedly that the $Zn(BIS\text{-}TRIS)^{2+}$ complexes exist in the form of several isomers. For the case of coordinating with maximal possible number of hydroxyl groups, the tentative structure of $Zn(BIS\text{-}TRIS)^{2+}$ is assumed as depicted in Figure S1. [27] [28] During the plating process, the coordinated Zn^{2+} with a high steric hindrance can block the active sites and the diffusion capability is strictly limited, leading to a uniform Zn deposition. Furthermore, partial substitution of water in solvation shell with organic molecule regulates the water content in the inner Helmholtz plane (IHP), which greatly suppresses the competitive HER and prevents the formation of the insulating by-products. As a consequence, with the addition amount of 0.1 M, a long-life Zn anode with up to more than 1000 h at a current density of 1 mA cm^{-2} and an area capacity of 1 mAh cm^{-2} is achieved based on such collaborative roles. Moreover, the

effectiveness of this strategy is further validated in an aqueous Zn/MnO_2 battery that delivers an 86% capacity retention after 600 cycles at 500 mA g^{-1}.

2. Experimental section

Preparation of MnO_2 cathode material: Briefly, 1.60 g $KMnO_4$ was dissolved into 20 ml deionized water. After 30 min of magnetic stirring, solution of $Mn(CH_3COO)_2{\cdot}4H_2O$ (0.720 g, 80 ml) was slowly added into solution of $KMnO_4$ with magnetic stirring for another 30 min. After being kept at 80 ^oC for 6 h, the dark precipitate was then collected by thoroughly centrifugation and washed several times with deionized water before drying at 80 ^oC for 12 h.

Material characterization: Phase structures of zinc foil and by-products were assessed by the X-ray diffraction analyzer (XRD, Bruker D8 diffractometer) at a scan rate of 1^o min^{-1}. The LabRAM HR evolution was carried out to investigate the coordination environment of Zn^{2+}. The surface structure of zinc foil after cycling/deposition was characterized by scanning electron microscopy (SEM, Hitachi S-4800). The ZW-C200 optical microscope was adopted to in situ investigate the zinc deposition.

Electrochemical test: The electrochemical performance of Zn/MnO_2 batteries were carried out by employing CR2025 coin-type cell, which is composed of a cathode electrode, a piece of Zn foil as counter electrode and Whatman glass fiber as separator. For the preparation of cathode material, MnO_2, Ketjen black and polyvinylidene fluoride (PVDF) were mixed with a mass ratio of 7:2:1. The N-methyl pyrrolidinone (NMP) was added into the mixture and the slurry was then casted onto Ti foil (0.01 mm). The average mass loading of active material was around 1.5 mg cm^{-2}. The Linear polarization and chronoamperometry (CAs) measurements were performed in three-electrode configuration, in which Zn plates were assembled as working and counter electrode, and saturated calomel (SCE) was used as reference electrode. The typical liquid electrolyte comprised 2 M $ZnSO_4$. For the BIS-TRIS contained electrolyte, 0.1 M BIS-TRIS was dissolved into it. The galvanostatic measurements were performed by Neware BTS-

5 battery test system. The cyclic voltammetry (CV) and electrochemical impedance spectroscopy (EIS) measurements were carried out on the CHI604E electrochemical station.

DFT calculation: Density Functional Theory (DFT) simulation was performed in Vienna ab initio simulation package (VASP) with the aid of projector augmented wave (PAW) method and the function of Perdew, Burke and Ernzerhof (PBE). The cutoff energy of 400 eV was used and a mesh of 1 ×1 × 1 in k-point grid was established for calculation. The Grimme's method (DFT-D3) was used and simulated system was fully relaxed only when the corresponding force was less than 0.01 eV $Å^{-1}$. The interaction energy (ΔE) between the Zn and specific molecular was calculated based on the equation as follows:

$$\Delta E = E_{system} - E_{Zn} - E_{molecular}$$

3. Results and Discussion

To verify this chelating chemistry induced regulation of solvation structure of Zn^{2+}, DFT calculation is carried out to compare the interaction energies between Zn-H_2O and Zn-(BIS-TRIS) systems. As shown in **Figure 1**c, the interaction energy of Zn-(BIS-TRIS) system (-0.14 eV) is much lower than that between Zn and H_2O (-0.06 eV), indicating that the binding affinity between Zn and BIS-TRIS is stronger than Zn-H_2O. Hence Zn tends to interact with chelator rather than molecular H_2O. The differential charge density further proves that comparing with Zn-H_2O system (Figure S2), electron interaction is enhanced for Zn-(BIS-TRIS) system (**Figure 1**d). The accumulation or depletion of charge can be recognized for Zn-(BIS-TRIS) system, reflecting the electron transfer from chelator to Zn. The stronger interaction for Zn-(BIS-TRIS) system theoretically demonstrates the feasibility of proposed chelating chemistry. Raman spectroscopy is then utilized to assess solvation structure of Zn^{2+} in electrolyte with or without BIS-TRIS. It can be found that two peaks located at around 390 and 450 cm^{-1} are exhibited in $ZnSO_4$ solution, which is consistent with the previous reports (**Figure 1**e). The Raman band (*ca.* 390 cm^{-1}) can be attributed to the Zn-OH_2 vibration. [29] [30] Along with the addition of BIS-TRIS, a new peak located at 500 cm^{-1} appears while no signal is detected in

pure BIS-TRIS solution between 450-550 cm^{-1} (Figure S3). It is worth noting that peak around 500 cm^{-1} can also be observed for N-doped ZnO (ca. 510 cm^{-1}). Therefore, the new peak in this realm may related to Zn-N mode and the shifting to a lower wavenumber may due to the formation of Zn-N-C. [31] [32] [33] The presence of new peak indicates the interaction between the Zn^{2+} and BIS-TRIS, which means that solvation structure of Zn^{2+} is altered with the addition of BIS-TRIS. [28] To further explore the change in solvation structure of Zn^{2+}, the variation of Raman band *v*-SO_4^{2-} is investigated. In terms of the association degree between the Zn^{2+} and SO_4^{2-}, there are two forms of solvation structure, solvent-separated ion pair (SIP, [Zn^{2+}-$(H_2O)_6{\cdot}SO_4^{2-}$]) and contact ion pair (CIP, [Zn^{2+}-$(H_2O)_5{\cdot}OSO_3^{2-}$], **Figure 1**b). [29] [34] In 2 M $ZnSO_4$ solution, the SIP specie and CIP account for 54% and 46% respectively, as being calculated from the peak area ratio (**Figure 1**f). As the concentration of BIS-TRIS increases, the *v*-SO_4^{2-} band shifts to lower frequency and the solvation structure of CIP is significant suppressed, which suggests that the SO_4^{2-} specie is difficult to participate the construction of inner sphere complexes in BIS-TRIS solution with higher concentration. This phenomenon further proves that the coordination environment of Zn^{2+} can be regulated effectively by the cheating agent BIS-TRIS

Typically, the effects of electrolyte additive on suppressing dendrite growth and side reactions are concentration-dependent. [35] In this work, we consider the ionic conductivity and corrosion behavior to optimize the concentration of selective additive and investigate the concentration effect of BIS-TRIS. Figure S4 shows the EIS results tested in the electrolyte with BIS-TRIS of 0, 0.05, 0.1 and 0.2 M. As it can be seen, the ionic conductivity is decreased with the addition of BIS-TRIS. Furthermore, the corrosion currents of zinc in various electrolytes are calculated by Tafel fitting of the linear polarization (Figure S5, Table S1). The lower current density indicate that the corrosion of zinc gets well alleviated in BIS-TRIS contained electrolyte. It should be noted that excessive BIS-TRIS additive cannot further lower down the corrosion density but significantly reduces the ionic conductivity. Hence, the optimal BIS-TRIS

concentration of 0.1 M is selected to investigate its role in realizing reversible Zn anode. **Figure 2**a-b show the surface morphologies of Zn foil after soaking in different electrolytes for a week. In bare $ZnSO_4$ electrolyte, rough surface with flaky by-products is observed which can be ascribe to the corrosion of metal Zn with moisture and oxygen. [36] On the contrary, metal Zn in BIS-TRIS contained electrolyte shows more slippery surface.

To further verify the compatibility of BIS-TRIS contained electrolyte with Zn electrode, *in situ* analysis of Zn deposition in a home-made cell is performed under optical microscopy, and real-time images are depicted in **Figure 2**f-g and Figure S6. After cycling at a current density of 1 mA cm^{-2} and a specific capacity of 1 mAh cm^{-2} for 2 cycles, bubbles have been observed at the electrode/electrolyte interface in bare $ZnSO_4$ electrolyte. The competitive hydrogen evolution not only induce low deposition/stripping Coulombic efficiency (CE), but also increase the internal pressure which will greatly affect the battery life in the practical use. In comparison, a dendrite-free Zn layer is uniformly deposited on the surface of Zn in BIS-TRIS contained electrolyte and no obvious bubble is detected. Furthermore, after cycling at 1 mA cm^{-2} for 1 mAh cm^{-2}, no peaks associated with by-products is detected in BIS-TRIS contained electrolyte, while in bare $ZnSO_4$ electrolyte, peaks located at 16.2, 22.4, 34.4, 50.1° are observed, corresponding to the by-products such as $Zn_4SO_4(OH)_6{\cdot}xH_2O$ (**Figure 2**e). [37] As depicted in **Figure 2**c, after cycling for 10 cycles, the Zn electrode in bare $ZnSO_4$ electrolyte shows a rough surface with numerous flaky products, while the Zn surface in BIS-TRIS contained electrolyte still remains smooth **(Figure 2**d). Hence, it can be concluded that the chemical/electrochemical stability of Zn metal is greatly improved in BIS-TRIS contained electrolyte, characterized chiefly by reduced corrosion rate, suppressed H_2 evolution and minimized generation of by-products. The higher stability of Zn can be attributed that the coordinated Zn-complex will participate the construction of double electrical layer, leading to the decrease of water content around the metal surface, which greatly suppress the competitive HER and hence prevent the formation of insulating by-products. [38] [24]

As being observed by *in situ* optical microscopy, the deposition of Zn in BIS-TRIS contained electrolyte features a unique dendrite-free property with smooth surface. To further identify the role of BIS-TRIS contained electrolyte on Zn deposition, the Ti foil and Cu wire are selected as substrates and the corresponding deposition surface morphologies in different electrolytes are compared. After depositing at a current density of 0.5 mA cm^{-2} and a specific areal capacity of 3 mAh cm^{-2}, the Ti in $ZnSO_4$ exhibits an obvious crack surface while the Ti in BIS-TRIS contained electrolyte shows a smoother surface, which plays an important role in the inhibition of dendrite growth (**Figure 3**a-b). As the case of the Cu wire with the diameter of ~2.2 mm as substrate, when the current is increased to 10 mA, a dendritic deposition of zinc is observed in $ZnSO_4$ as shown in **Figure 3**c while a spherical structured zinc deposition is achieved in BIS-TRIS contained electrolyte (**Figure 3**d). In order to elucidate the impact of BIS-TRIS additive on the electrochemical interfacial properties at Zn electrode, various rate cyclic voltammetry (CV) is used to investigate the corresponding adsorption properties (Figure S7). It is clearly seen that BIS-TRIS additive lowers the double layer capacitance at Zn metal surface. The decrease in double layer capacitance can be ascribed to the adsorption of $Zn(BIS\text{-}TRIS)^{2+}$ complex which has high steric hindrance. [39] For $ZnSO_4$ electrolyte, when initial Zn nucleation sites evolve into protuberances, zinc ions intend to migrate to the tip site whereas edge sites of protuberances are scarcity of zinc ions, inducing deposition of dendritic structure as illustrated in **Figure 3**f.[16] While in BIS-TRIS contained electrolyte, the zinc ions are coordinated with hydroxyl group of BIS-TRIS. Therefore, when zinc complexes are adsorbed on the tip sites under the electric field, the preference sites would be blocked. Therefore, the distribution of zinc complexes on the protuberances appear to be more uniform, leading to the spherical Zn deposition (**Figure 3**e). [40]

To understand the dendritic inhibiting mechanism, the kinetic of Zn deposition in different electrolytes are evaluated. Galvanostatic cycling test of symmetric cells in different electrolyte

are conducted at various current density (Figure S8). Hence, the exchange current density can be calculated according to the following equation [1]: [41] [37]

$$i \approx i_0 \frac{F}{RT} \frac{\eta}{2} \quad [1]$$

Based on the relationship between the overpotential (η) and current density (*i*), the exchange current density (i_0) can be calculated. As depicted in **Figure 3**g, the deposition in BIS-TRIS-contained electrolyte shows a lower exchange current density of 5.2 mA cm^{-2} in comparison to that in $ZnSO_4$ electrolyte (9 mA cm^{-2}). It is generally believed that dendrite growth rate is closely related with the zinc electrodeposition kinetic and lowering the exchange current density can strengthen the dendrite suppression. [42]

Moreover, the cyclic voltammetry (CV) curves of Zn deposition with Ti foil as substrate are compared to investigated the initial nucleation behaviors of Zn. As shown in **Figure 3**h, the point A represents the potential where Zn^{2+} starts to be reduced and the potential difference between the point A and B represents the nucleation overpotential. When adding BIS-TRIS additive into electrolyte, the reduction potential is changed from A to A' and the nucleation overpotential is increased by 20 mV, which means that BIS-TRIS degrades the deposition kinetic of zinc. This can be attributed to the stronger steric hindrance of zinc complex, which blocks the sites for rapid growth. The slowed zinc reduction rate alleviates the concentration polarization during the deposition process, resulting into the uniform distribution of Zn^{2+} near the metal surface. [16] Moreover, from the chronoamperometry results shown in Figure S9, the current density shows negligible change beyond initial 100 s in BIS-TRIS electrolyte, which suggests the constrained 2D surface diffusion of zinc complexes. [23] [43] On account of the uniformly distributed of Zn^{2+} and constrained 2D surface diffusion, the zinc ions are prone to deposit locally. Thus, dendrite growth is well suppressed and an even deposition layer is formed.

To evaluate the cycling stability of Zn anode in BIS-TRIS contained electrolyte, galvanostatic cycling test of symmetric cell is conducted at various current densities. As shown

in **Figure 4**a, the cell in BIS-TRIS contained electrolyte shows a larger overpotential, which is in a good consistence with the lower kinetic in BIS-TRIS contained electrolyte as discussed above. After cycling at 1 mA cm^{-2} with a specific capacity of 1 mAh cm^{-2} for about 220 h, the cell in $ZnSO_4$ electrolyte shows explicit voltage fluctuation and the weak voltage response reflects the short circuit in the cell, which may be associated with the uncontrolled dendrite growth. From the SEM images of symmetric cells after cycling at a current density of 1 mA cm^{-2} and an area capacity of 1 mAh cm^{2-} for 150 cycles, the Zn metal in $ZnSO_4$ is totally smashed to pieces. While, for BIS-TRIS contained electrolyte, the smooth surface is maintained, though small flakes are also observed (Figure S10). Hence, the cell in BIS-TRIS contained electrolyte shows superior cycling stability up to over 1200 h with no obvious voltage fluctuation detected. When increasing the current density to 5 mA cm^{-2} and the capacity to 5 mAh cm^{-2}, the cell in BIS-TRIS contained electrolyte still shows satisfied stability with more than 600 h, while short circuit occurs within initial 50 h for cell in $ZnSO_4$ electrolyte (**Figure 4**b). In consideration that zinc reversibility plays an important role in the practical use of rechargeable Zn-ion batteries, the CE test in Zn//Ti cell is conducted to evaluate the zinc plating/stripping efficiency (**Figure 4**c). After 30 cycles of stable plating/stripping process, the cell in $ZnSO_4$ electrolyte shows sharp fluctuation in CE and short-circuit failure occurs in the 55^{th} cycles (**Figure 4**d). In contrast, the cell with BIS-TRIS contained electrolyte shows a stable CE characteristic of 98.5%, across the nearly 400 process cycles of Zinc plating/stripping. This excellent stability reveals the fact that the BIS-TRIS additive can greatly suppress the side reactions and dendrite formation which easily leads to the formation of "dead Zn".

To evaluate the practical use of BIS-TRIS contained electrolyte, Zn/MnO_2 batteries with different electrolytes are assembled and tested. $MnSO_4$ is added to suppress the dissolution of Mn^{2+} from the MnO_2 cathode for all samples (Figure S11). [44] [45] From the cyclic voltammetry (CV) curves (**Figure 5**a), it can be seen that MnO_2 in the BIS-TRIS contained electrolyte shows

similar electrochemical behaviors as that in the $ZnSO_4$ electrolyte, suggesting that altered zinc coordination does not affect the redox process of MnO_2. Likewise, two cells show similar galvanostatic charge/discharge curves in **Figure 5**b-c. The discharge capacity of 260 mAh g^{-1} is obtained in $ZnSO_4$ electrolyte, which is higher than that in BIS-TRIS contained electrolyte (about 200 mAh g^{-1}). In order to understand this phenomenon, activation energy calculation based on Arrhenius equation is performed to investigate the energy consumption for the Zn^{2+} de-solvation (Figure S12). Besides the slightly increase of the charge transfer resistance (R_{ct}), the activation energy of cell with BIS-TRIS additive is calculated to be 66.68 kJ mol^{-1} which is higher than that in $ZnSO_4$ electrolyte, suggesting the affected transfer kinetic by additive (Figure S13). Herein, the capacity sacrifice of the Zn/MnO_2 battery in BIS-TRIS electrolyte can be attributed to the de-solvation barrier increase of Zn^{2+} at the cathode side. [37] [46] [47] After cycling at 500 mA g^{-1} for 600 cycles, a discharge capacity above 200 mAh g^{-1} is maintained in BIS-TRIS contained electrolyte. The capacity increases steadily in the later period, which is a relatively common phenomenon for Mn-based system. Such a gradual activation can possibly be attributed to two reasons. First, the electrolyte gradually soaks through the cathode material during the cycling. Second, the pre-added $MnSO_4$ in the electrolyte may deposited on the cathode electrode, which provides the extra active sites. [48] [49] Contrary, the full cell in $ZnSO_4$ electrolyte suffers from serious capacity degradation, which may be attributed to the severe corrosion and side reactions on the Zn anode **(Figure 5**d**)**. In order to further demonstrate the reversibility of Zn anode, Zn foil with the thickness of 1μm is selected as anode and the theoretical capacity ratio of Zn to MnO_2 is about 7:1 (7.0x excess Zn based on active mass). It is also found that the cell with BIS-TRIS contained electrolyte shows better electrochemical performance, further verifying the better stability of Zn anode with the additive of BIS-TRIS (Figure S14). The above results demonstrate the promises of BIS-TRIS in achieving the long-life Zn-ion battery**.**

4. Conclusion

In summary, we demonstrated a dendrite-free and side reaction suppressed Zn anode with BIS-TRIS as electrolyte additive, which contains abundant hydroxyl group to coordinate with Zn^{2+}. The zinc-complex with stronger steric hindrance are demonstrated to elevate the nucleation barrier and the slowed deposition rate alleviates the concentration polarization during cycling. Moreover, the constricted 2D diffusion during deposition prevents the aggregation of zinc ions on energetical favorable sites, thus significantly suppressing the dendrite growth and generating a uniform Zn layer. In addition, partial substitution of water in solvation shell with BIS-TRIS additive regulate the water content near the metal surface, which plays an important role in enhancing the chemical/electrochemical stability of Zn metal. Accordingly, a highly reversible plating/stripping with an average CE of 98.5% is achieved and for symmetric cell, and a lifespan over 1200 h is obtained at 1 mA cm^{-2} for a specific capacity of 1 mAh cm^{-2}. The practical operability of BIS-TRIS contained electrolyte is further validated by the Zn/MnO_2 full cell that shows neglected capacity decay even after cycling at 500 mA g^{-1} for over 600 cycles. This BIS-TRIS chelating strategy in realizing dendrite-free Zn anode is hoped to accelerate the transition to scalable application for ZIB.

References

[1] X. Jia, C. Liu, Z. G. Neale, J. Yang, G. Cao, *Chem. Rev.* **2020**, *120*, 7795.

[2] L. E. Blanc, D. Kundu, L. F. Nazar, *Joule* **2020**, *4*, 771.

[3] B. Tang, L. Shan, S. Liang, J. Zhou, *Energy Environ. Sci.* **2019**, *12*, 3288.

[4] J. Gao, X. Xie, S. Liang, B. Lu, J. Zhou, *Nano-Micro Lett.* **2021**, *13,* 69.

[5] M. Winter, R. J. Brodd, *Chem. Rev.* **2004**, *104*, 4245.

[6] L. Fang, C. Wang, L. Huangfu, N. Bahlawane, H. Tian, Y. Lu, H. Pan, M. Yan, Y. Jiang, *Adv. Funct. Mater.* **2019**, *29*, 1906680.

[7] J. Huang, J. Zhou, S. Liang, *Acta Phys. -Chim. Sin*. **2021**, *37*, 2005020.

[8] M. Luo, H. Yu, F. Hu, T. Liu, X. Cheng, R. Zheng, Y. Bai, M. Shui, J. Shu, *Chem. Eng.*

J. **2020**, *380*, 122557.

[9] W. Guo, Z. Cong, Z. Guo, C. Chang, X. Liang, Y. Liu, W. Hu, X. Pu, *Energy Storage Mater.* **2020**, *30*, 104.

[10] T. Shoji, M. Hishinuma, T. Yamamoto, *J. Appl. Electrochem.* **1988**, *18*, 521.

[11] T. Yamamoto, T. Shoji, *Inorg. Chim. Acta* **1986**, *117*, L27.

[12] T. Shoji, T. Yamamoto, *J. Electroanal. Chem.* **1993**, *362*, 153.

[13] C. Xu, H. Du, B. Li, F. Kang, Y. Zeng, *Electrochem. Solid-State Lett.* **2009**, *12*, A61.

[14] C. Xu, B. Li, H. Du, F. Kang, *Angew. Chem., Int. Ed.* **2012**, *51*, 933.

[15] C. Xu, S. W. Chiang, J. Ma, F. Kang, *J. Electrochem. Soc.* **2012**, *160*, A93.

[16] W. Lu, C. Xie, H. Zhang, X. Li, *ChemSusChem* **2018**, *11*, 3996.

[17] Q. Yang, Q. Li, Z. Liu, D. Wang, Y. Guo, X. Li, Y. Tang, H. Li, B. Dong, C. Zhi, *Adv. Mater.* **2020**, *32*, 2001854.

[18] J. Hao, X. Li, X. Zeng, D. Li, J. Mao, Z. Guo, *Energy Environ. Sci.* **2020**, *13*, 3917.

[19] Q. Zhang, J. Luan, Y. Tang, X. Ji, H. Wang, *Angew. Chem., Int. Ed.* **2020**, *59*, 13180.

[20] X.-B. Cheng, R. Zhang, C.-Z. Zhao, Q. Zhang, *Chem. Rev.* **2017**, *117*, 10403.

[21] J. Hao, B. Li, X. Li, X. Zeng, S. Zhang, F. Yang, S. Liu, D. Li, C. Wu, Z. Guo, *Adv. Mater.* **2020**, *32*, 2003021.

[22] L. Cao, D. Li, T. Deng, Q. Li, C. Wang, *Angew. Chem., Int. Ed.* **2020**, *59*, 19292.

[23] Z. Zhao, J. Zhao, Z. Hu, J. Li, J. Li, Y. Zhang, C. Wang, G. Cui, *Energy Environ. Sci.* **2019**, *12*, 1938.

[24] F. Wang, O. Borodin, T. Gao, X. Fan, W. Sun, F. Han, A. Faraone, J. A. Dura, K. Xu, C. Wang, *Nat. Mater.* **2018**, *17*, 543.

[25] R. Qin, Y. Wang, M. Zhang, Y. Wang, S. Ding, A. Song, H. Yi, L. Yang, Y. Song, Y. Cui, J. Liu, Z. Wang, S. Li, Q. Zhao, F. Pan, *Nano Energy* **2021**, *80*, 105478.

[26] B. Li, Z. Nie, M. Vijayakumar, G. Li, J. Liu, V. Sprenkle, W. Wang, *Nat. Commun.* **2015**, *6*, 6303.

[27] K. H. Scheller, T. H. J. Abel, P. E. Polanyi, P. K. Wenk, B. E. Fischer, H. Sigel, *Eur. J. Biochem.* **1980**, *107*, 455.

[28] D. J. Wesolowski, D. A. Palmer, G. M. Begun, *J. Solution Chem.* **1990**, *19*, 159.

[29] H. Yang, Z. Chang, Y. Qiao, H. Deng, X. Mu, P. He, H. Zhou, *Angew. Chem., Int. Ed.* **2020**, *59*, 9377.

[30] W. W. Rudolph, M. H. Brooker, P. R. Tremaine, *J. Solution Chem.* **1999**, *28*, 621.

[31] F. Friedrich, N. H. Nickel, *Appl. Phys. Lett.* **2007**, *91*, 111903.

[32] X. Zhu, H.-Z. Wu, D.-J. Qiu, Z. Yuan, G. Jin, J. Kong, W. Shen, *Opt. Commun.* **2010**, *283*, 2695.

[33] L. L. Kerr, X. Li, M. Canepa, A. J. Sommer, *Thin Solid Films* **2007**, *515*, 5282.

[34] W. R. Wolfram, H. B. Murray, T. Peter, *Z. Phys. Chem.* **1999**, *209*, 181.

[35] Q. Zhang, J. Luan, L. Fu, S. Wu, Y. Tang, X. Ji, H. Wang, *Angew. Chem., Int. Ed.* **2019**, *58*, 15841.

[36] J. Hao, X. Li, S. Zhang, F. Yang, X. Zeng, S. Zhang, G. Bo, C. Wang, Z. Guo, *Adv. Funct. Mater.* **2020**, *30*, 2001263.

[37] X. Xie, S. Liang, J. Gao, S. Guo, J. Guo, C. Wang, G. Xu, X. Wu, G. Chen, J. Zhou, *Energy Environ. Sci.* **2020**, *13*, 503.

[38] C. Zhang, J. Holoubek, X. Wu, A. Daniyar, L. Zhu, C. Chen, D. P. Leonard, I. A. Rodríguez-Pérez, J.-X. Jiang, C. Fang, X. Ji, *Chem. Commun.* **2018**, *54*, 14097.

[39] Y. Jin, K. S. Han, Y. Shao, M. L. Sushko, J. Xiao, H. Pan, J. Liu, *Adv. Funct. Mater.* **2020**, *30*, 2003932.

[40] X.-R. Chen, Y.-X. Yao, C. Yan, R. Zhang, X.-B. Cheng, Q. Zhang, *Angew. Chem., Int. Ed.* **2020**, *59*, 7743.

[41] J. Lopez, A. Pei, J. Y. Oh, G.-J. N. Wang, Y. Cui, Z. Bao, *J. Am. Chem. Soc.* **2018**, *140*, 11735.

[42] S. J. Banik, R. Akolkar, *J. Electrochem. Soc.* **2013**, *160*, D519.

[43] A. Bayaguud, X. Luo, Y. Fu, C. Zhu, *ACS Energy Lett.* **2020**, *5*, 3012.

[44] H. Pan, Y. Shao, P. Yan, Y. Cheng, K. S. Han, Z. Nie, C. Wang, J. Yang, X. Li, P. Bhattacharya, K. T. Mueller, J. Liu, *Nat. Energy* **2016**, *1*, 16039.

[45] Y. Zhao, Y. Zhu, X. Zhang, *InfoMat* **2020**, *2*, 237.

[46] D. Kundu, S. Hosseini Vajargah, L. Wan, B. Adams, D. Prendergast, L. F. Nazar, *Energy Environ. Sci*. **2018**, *11*, 881.

[47] C. Yan, H.-R. Li, X. Chen, X.-Q. Zhang, X.-B. Cheng, R. Xu, J.-Q. Huang, Q. Zhang, *J. Am. Chem. Soc.* **2019**, *141*, 9422.

[48] Y. Fu, Q. Wei, G. Zhang, X. Wang, J. Zhang, Y. Hu, D. Wang, L. Zuin, T. Zhou, Y. Wu, S. Sun, *Adv. Energy Mater*. **2018**, *8*, 1801445.

[49] B. Wu, G. Zhang, M. Yan, T. Xiong, P. He, L. He, X. Xu, L. Mai, *Small* **2018**, *14*, 1703850.

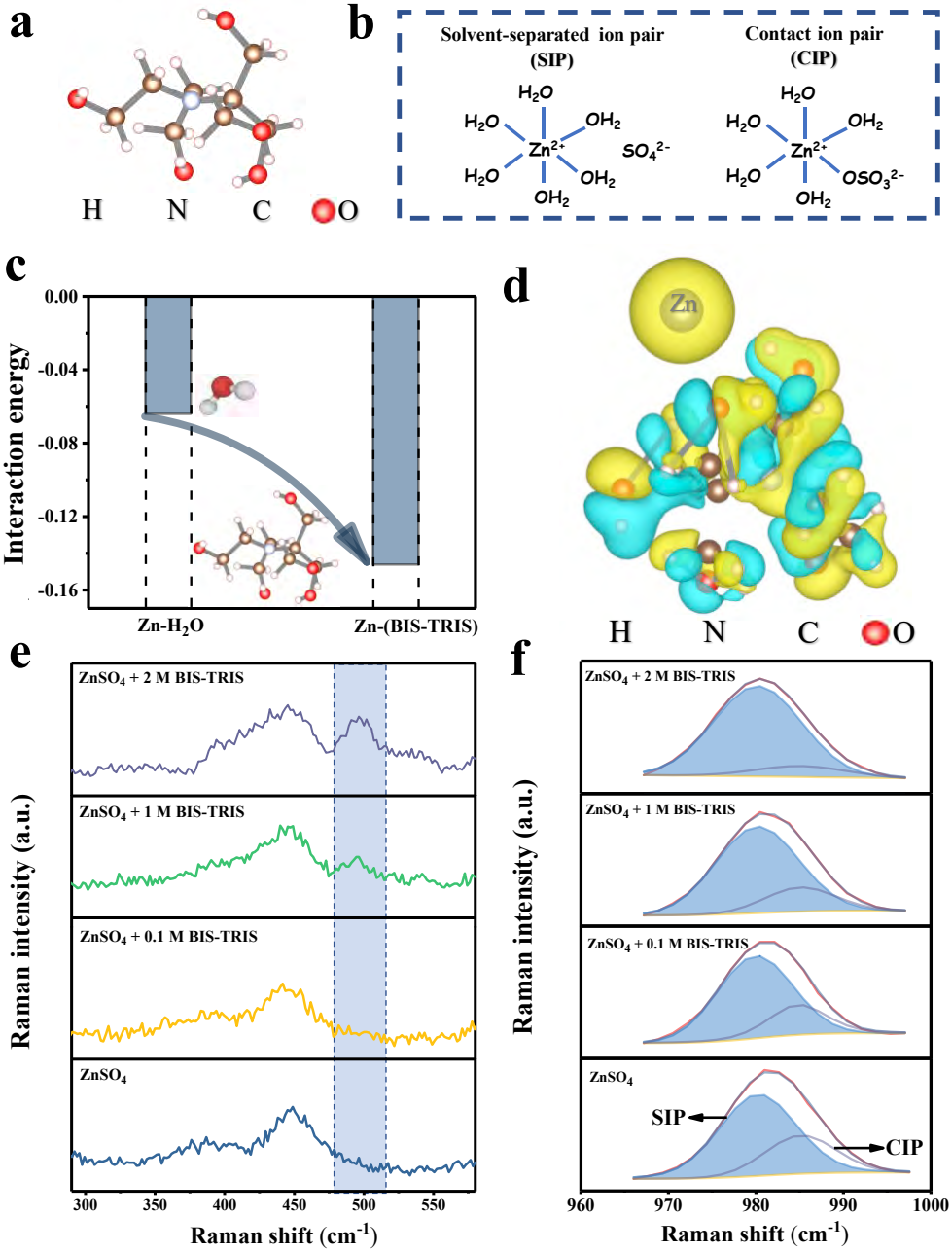

Figure 1. (a) Molecular structure of chelator BIS-TRIS. (b) Schematic illustration of two solvation structures in $ZnSO_4$ solution in view of the association degree between the Zn^{2+} and SO_4^{2-}. (c) The calculated interaction energy of Zn-H_2O and Zn-(BIS-TRIS). (d) Differential charge density of Zn-(BIS-TRIS) system. The yellow/blue areas represent an increase/decrease of the electron density. Raman spectra of $ZnSO_4$ with varying BIS-TRIS concentrations: (e) $\nu_{Zn\text{-}O}$ and (f) $\nu_{SO_4^{2-}}$

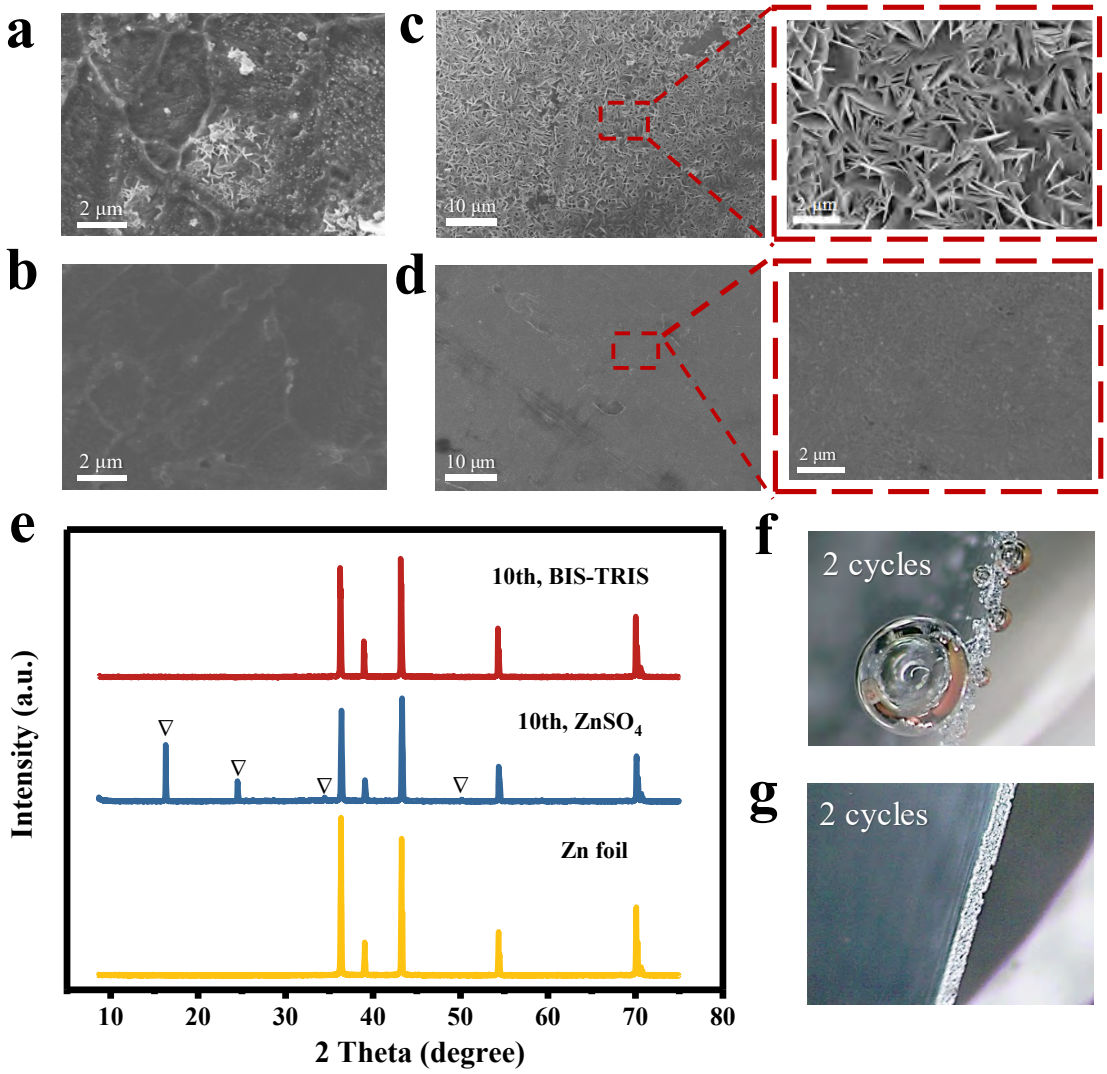

Figure 2: The surface morphologies of commercial zinc foil after soaking in (a) $ZnSO_4$ electrolyte and (b) BIS-TRIS contained electrolyte for 7 days. SEM images of Zn anode after cycling in (c) $ZnSO_4$ electrolyte and (d) BIS-TRIS contained electrolyte for 10 cycles. (e) XRD patterns of zinc anode before and after cycling in different electrolytes for 10 cycles. In situ optical microscopic images of Zn electrode cycling at 1 mA cm^{-2} for 1 mAh cm^{-2} in (f) $ZnSO_4$ electrolyte and (g) BIS-TRIS contained electrolyte.

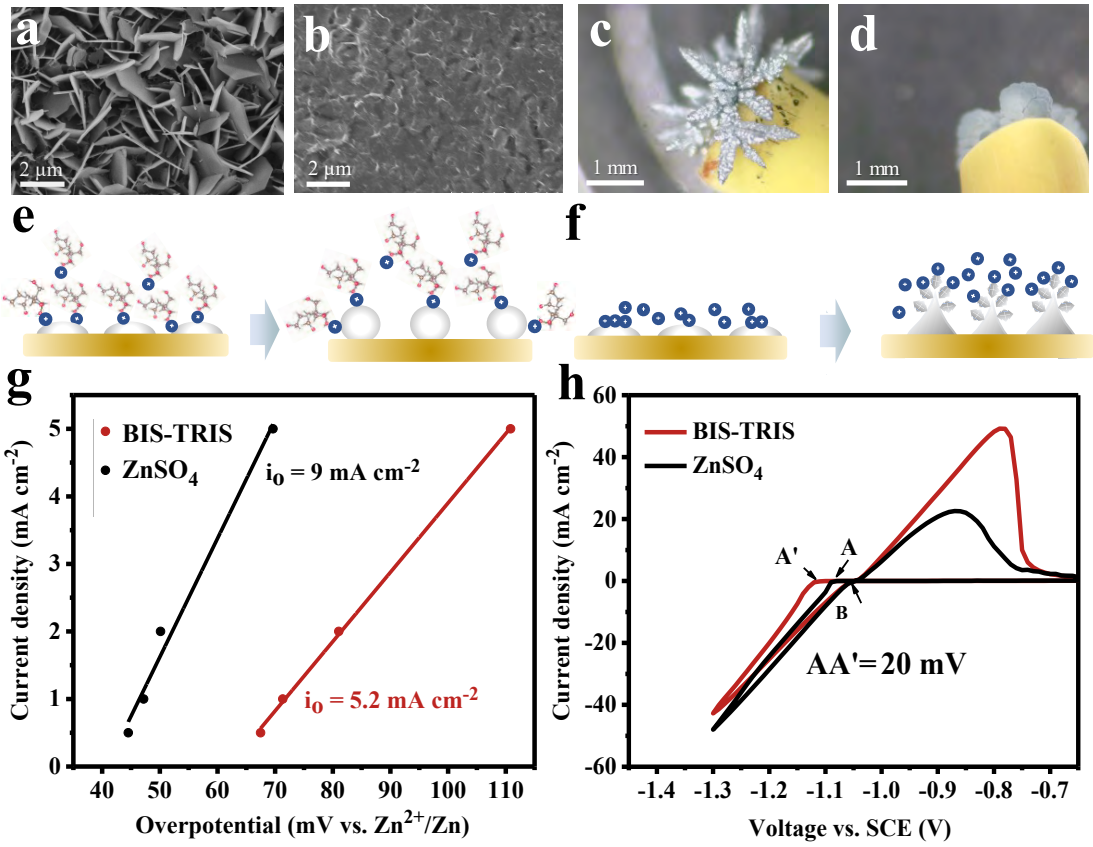

Figure 3. SEM images of Zn deposition on Ti foil in (a) $ZnSO_4$ electrolyte and (b) BIS-TRIS contained electrolyte at a current density of 0.5 mA cm^{-2} and an area capacity of 3 mAh cm^{-2}. Optical microscopy of Zn deposition on Cu wire in (c) $ZnSO_4$ electrolyte and (d) BIS-TRIS contained electrolyte at a current density of 10 mA. Scheme illustration of (e) spherical Zn deposition in BIS-TRIS contained electrolyte and (f) dendritic Zn deposition in $ZnSO_4$ electrolyte. (g) Calculated exchange density of Zn asymmetric cell with different electrolytes. (h) Cyclic voltammograms (CV) for Zn nucleation on bare Ti foil in $ZnSO_4$ and BIS-TRIS contained electrolytes.

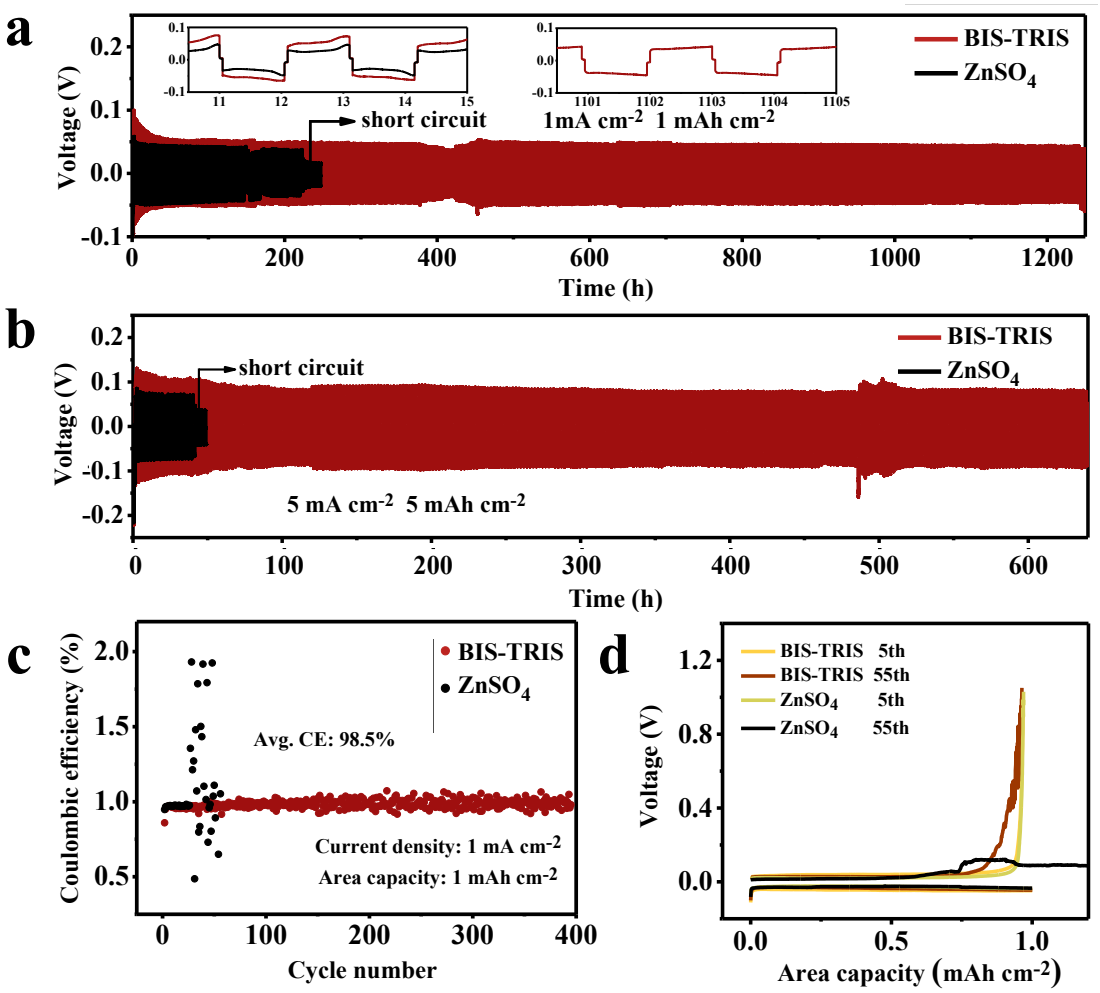

Figure 4. (a) Galvanostatic cycling test of symmetric cell at a current density of (a) 1 mA cm^{-2} and (b) 5 mA cm^{-2}. (c) CE of Zn plating/stripping on Ti foil at a current density of 1 mA cm^{-2}. (d) The corresponding voltage profiles at various cycles.

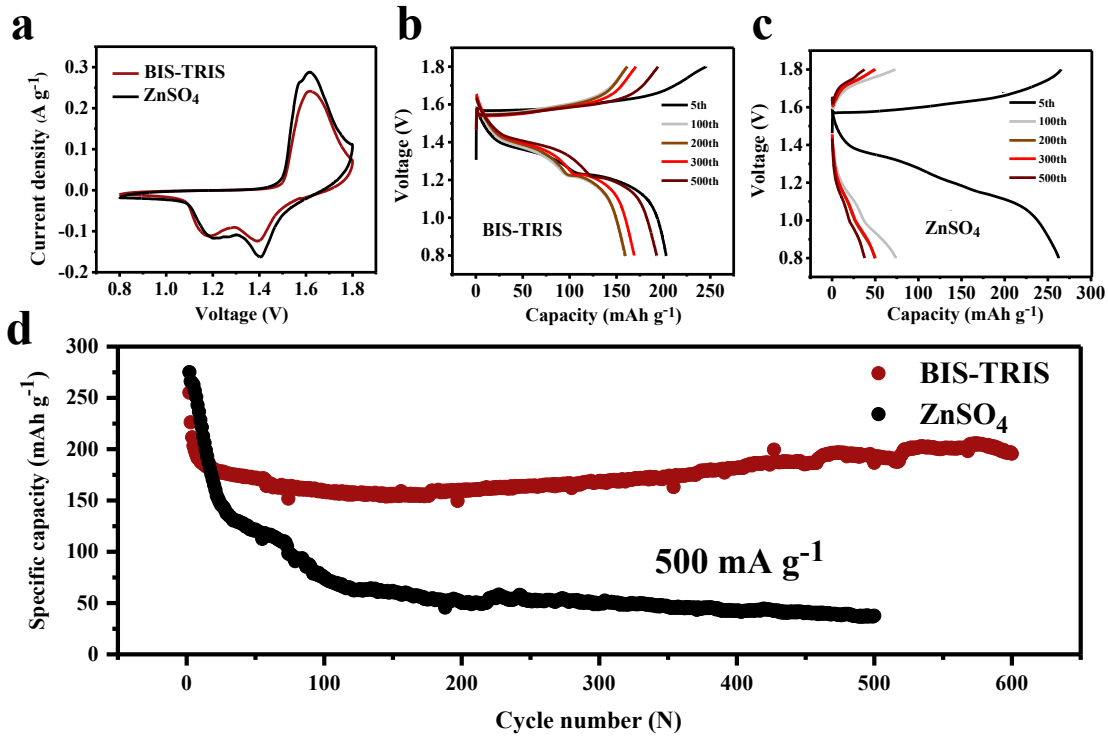

Figure 5: Electrochemical performance of Zn/MnO_2 batteries: (a) cyclic voltammetry (CV) measurement, (b, c) the galvanostatic charge/discharge curves at various cycles and (d) cycling performance at 500 mA g^{-1}